



Synthesis of lipophilic gold nanorod superparticles and their size-dependent SERS performances

Gui-Lin Wu · Tian-Song Deng · Kun-Peng Wang ·
Er-Ji Zhang · Li-Yong Liu · Yu-Chun Cheng ·
Jia-Fei Gao · Jie Liu

Received: 14 September 2024 / Accepted: 6 January 2025
© The Author(s), under exclusive licence to Springer Nature B.V. 2025

Abstract Gold nanorods are widely used in surface-enhanced Raman scattering (SERS) applications due to their strong localized surface plasmon resonance (LSPR). The self-assembly of gold nanorods further expands their applications and introduces new ensemble properties. In this paper, two types of gold nanorods with similar lengths but significantly different diameters were used for making superparticles. The gold nanorods were first surface-modified with thiol-terminated polystyrene (PS-SH), and then assembled into superparticles through emulsion volatilization. To test the SERS performances of the gold nanorod superparticles, Nile red was used as a dye molecule to test the localization of the SERS performance of the single superparticles. It was found that as the size of the superparticles increased, the SERS performances also improved, with the final Raman signal intensity reaching up to 2×10^6 . When the size of the superparticles was the same, the SERS performance was stronger for superparticles composed of gold nanorods with larger diameters. Additionally, a

structure similar to the superparticles was designed for FDTD simulations, and the simulated results were highly consistent with the experimental results, further supporting our conclusions.

Keywords Gold nanorods · Superparticles · Thiol-terminated polystyrene · SERS · FDTD simulations · Plasmon resonance · Self-assembly

Introduction

Raman detection technology can non-destructively analyze the chemical structure, morphology, crystallinity, and interactions of substances [1–3]. However, the Raman spectrum of the object itself is often particularly weak, making Raman detection technology very challenging [4]. In recent years, increasing attention has been paid to the surface-enhanced Raman scattering (SERS) technique, which can increase the intensity of the Raman spectrum by several orders of magnitude [5–7]. The most commonly used approach involves using precious metal nanoparticles as SERS substrates, which enhance Raman scattering through the localized surface plasmon resonance (LSPR) properties of the nanoparticles [8–12].

The LSPR of noble metal nanoparticles is highly dependent on their morphology [13]. However, due to the limited morphology of individual nanoparticles and the difficulties in synthesizing them [14], research has gradually focused on the self-assembly

Supplementary Information The online version contains supplementary material available at <https://doi.org/10.1007/s11051-025-06216-2>.

G.-L. Wu · T.-S. Deng (✉) · K.-P. Wang · E.-J. Zhang ·
L.-Y. Liu · Y.-C. Cheng · J.-F. Gao · J. Liu
School of Electronics and Information Engineering,
Hangzhou Dianzi University, Hangzhou 310018,
P. R. China
e-mail: dengts@pku.edu.cn

of nanoparticles. In the assembled nanostructures, there were plasmonic coupling effect between nanoparticles' positioned gap less than 10 nm [15–18], which generates a strong electric field in the interstices of the nanoparticles. This narrow and strong electric field is typically referred to as a SERS hotspot. Although the hotspot only occupies a small part of the entire SERS substrate [19–21], most of the enhancement comes from these hotspots, making the creation of more hotspots a key research focus. Additionally, when using precious metal nanoparticles as SERS substrates, their stability is crucial [22–24]. For example, gold nanoparticles can remain stable in water after CTAB surface modification and become lipophilic after thiol-terminated polystyrene (PS-SH) modification [25–28], allowing them to stabilize in oily liquids, such as toluene. Surface modification thus extends the application range of SERS for precious metal nanoparticles. Gold nanorods (GNRs) are widely used in SERS substrates primarily because they have strong LSPR properties in the visible and near infrared range [29, 30]. Additionally, the anisotropy of GNRs facilitates the generation of more SERS hotspots [31]. Over the years, research and development have led to mature methods for growing GNRs, with many synthesis techniques now available to produce GNRs with good monodispersity [32]. This advancement provides a solid foundation for the self-assembly of GNRs, as high-purity gold nanoparticles are crucial for successful self-assembly, especially for ordered structures [33].

In recent years, significant progress has been made in the self-assembly of GNRs [34], with the most common method being the formation of gold nanorod arrays. For example, in 2021, Albarghouthi et al. utilized the self-assembly of GNRs to form two-dimensional arrays [35]. These nano-arrays, when used as SERS substrates, performed well in tests with para-aminothiophenol (p-ATP). However, the utility of 2D self-assembled structures as SERS substrates is limited due to the constant area available for assays [36, 37]. Only self-assembly in three dimensions can further enhance the SERS performance of these assemblies [38, 39]. Superparticles are structured particles assembled from smaller particles, forming a complex three-dimensional structure [40]. This increases the number of hotspots significantly [41]. In the self-assembly of superparticles from GNRs, Li et al. created superparticles with broadband absorption peaks

by self-assembling through emulsion evaporation after coating mesoporous silica on the surface of GNRs and modifying them with OTMOS [42]. However, their application in SERS is limited because the thick mesoporous silica layer on the surface of the GNRs restricts the interaction between the substrate and the target material, and the LSPR properties of the GNRs are partially weakened by the silica shell.

In this study, we used a simple method to form superparticles by employing the emulsion evaporation self-assembly method with surface-modified GNRs. We used two types of GNRs with different aspect ratios to form superparticles, aiming to explore the impact of the nanorod dimensions on SERS performances. Additionally, we tested the SERS performances of superparticles with different sizes formed from these two types of nanorods. The PS-SH-modified GNRs exhibited good binding with hydrophobic dyes, so we used Nile red as the dye in our experiments. By measuring the Raman signal intensity of Nile red, we observed that the Raman signal increased with the size of the superparticles. Moreover, when comparing superparticles of the same diameter but composed of GNRs with different aspect ratios, we found that superparticles made of larger diameter nanorods exhibited better SERS performances. To substantiate our findings, we conducted FDTD simulations. Despite the overall irregularity of the superparticle surfaces, many small regions formed arrays of GNRs, primarily arranged side-by-side. Based on this observation, we designed the structures for the simulations. The simulated results indicated that as the size of the simulated assemblies increased, the electric field strength around the GNRs also increased, and the number of SERS hotspots gradually increased. Since the increase in the size of the superparticles was not limited to the horizontal direction, we also increased the number of particles in the vertical direction in our simulations. We found that adding nanorods in the vertical direction significantly enhanced the electric field strength, which aligned well with our experimental results.

Experimental

All chemicals were used as received without further purification. Hexadecyltrimethylammonium bromide (CTAB, > 99.0%) was purchased from

TCI America. Chloroauric acid (HAuCl_4), L-ascorbic acid (AA, >99.99%, hydrochloric acid (HCl, 37 wt% in water), sodium dodecyl sulfate (SDS, 92.5–99%), dextran, rhodamine 6G (R6G, 95%), Nile red, and methanol (99.5%) were purchased from Shanghai Macklin Biochemical Technology Co., Ltd. Silver nitrate (AgNO_3 , >99.8%), sodium oleate (NaOL , >99.88%), sodium borohydride (NaBH_4 , >98%), and tetrahydrofuran (THF, 99.0%) were purchased from Shanghai Aladdin Biochemical Technology Co., Ltd. Thiol-terminated polystyrene (average $M_n=5000$, $\text{PDI}\leq 1.1$, named PS-SH-5 k) was purchased from Sigma-Aldrich. Thiol-terminated polystyrene (average $M_n=11000$, $\text{PDI}\leq 1.1$, named PS-SH-11 k) was purchased from MKCH2403. Toluene (TOL, $\geq 99.5\%$) was purchased from National Pharmaceutical Group Chemical Reagent Co., Ltd. Ultrapure water ($> 18.2 \text{ M}\Omega$) obtained from a Milli-Q water system was used in all experiments. All glassware were cleaned using freshly prepared aqua regia (HCl in a 3:1 ratio by volume) followed by rinsing with copious amounts of water.

Synthesis of GNRs

GNRs with aspect ratios of 3.5 and 6.0 were synthesized using a seed-mediated growth method [43]. First, the seed solution was synthesized. Specifically, 0.25 mL of 0.01 M HAuCl_4 solution was added to 10 mL of 0.1 M CTAB solution, then 0.6 mL of freshly prepared ice-cold 0.01 M NaBH_4 was added. The solution was stirred vigorously at 1200 rpm for 2 min, then the stirring was stopped. The color changed from golden yellow to brown, and the solution was left to stand for 30 min.

Next, the growth solution was prepared. Specifically, 7.0 g of CTAB and 1.24 g of NaOL were added to 400 mL of water. After complete dissolution and clarification of the solution, 24 mL (18 mL for aspect ratio 6) of 4 mM AgNO_3 solution and 25 mL of 0.01 M HAuCl_4 solution were added. The solution was stirred at 500 rpm for 90 min, during which it gradually became colorless, completing the preparation of the growth solution. Subsequently, 2.8 mL (4.8 mL for aspect ratio 6) of 12.1 M HCl was added to the growth solution. After stirring at 400 rpm for 15 min, 1.25 mL of 64 mM AA and 0.8 mL (0.4 mL for aspect ratio 6) of the seed solution were added. The solution was stirred at 1200 rpm for 1 min and

then left to stand overnight for 12 h to complete the growth process. The resulting gold nanorod solution was centrifuged at 8000 rpm and washed twice to obtain the final product. After removing the supernatant twice, the gold nanorod solution is finally dispersed in 500 mL of 1.5 mM CTAB aqueous solution (If subsequent purification is required, it is not necessary to perform two washes, but can be purified directly).

Purification of GNRs

The method was based on that proposed by Kyoungweon Park et al. with slight changes [33]. Due to the higher impurity content in GNRs with an aspect ratio of 6, further purification was required before use. Specifically, 21.7 g of CTAB (to be adjusted) was added to 250 mL of the synthesized gold nanorod solution (final concentration approximately 275 mM). After standing for 24 h, the supernatant was decanted to obtain the final product.

Surface modification of GNRs with PS-SH

A simple and efficient surface-modified method was used but with some improvements [28, 44]. First, 0.4 mg of PS-SH was dissolved in 2 mL of THF solution. Then, the synthesized GNRs (8 mL) were centrifuged and washed twice, concentrated to 200 μL , and added to the THF solution. After sonication for 90 min, PS-SH successfully replaced the original CTAB on the surface of the GNRs, completing the surface modification. The solution was then centrifuged at 8000 rpm and the supernatant was removed. Then, 5 mL of methanol was added, and centrifuged and washed again. Finally, 5 mL of toluene was added and the solution was centrifuged and washed once more to obtain the final product (5 k and 11 k molecular weight of PS-SH using the same procedure).

Self-assembly of GNRs-(PS-SH)

An emulsion volatilization self-assembly method was used for making superparticles [45]. Firstly, 80 mg of dextran and 3 mg of SDS were added to 2 mL of ultrapure water. After completely dissolving, the previously synthesized 5 mL of GNRs@PS-SH (in toluene) solution was concentrated to 150 μL and added to an aqueous emulsion. The solution was sonicated

at 40.0 kHz for 2 min. Then, let the solution stand at room temperature for 3 days to ensure complete evaporation of toluene. Finally, the solution was centrifuged at 5000 rpm once, then at 3000 rpm twice to obtain the final product, which was then dispersed in water.

SERS performances test for superparticles

Raman detection was performed using a LabRAM HR Evolution model system. The sample fabrication procedure was shown in Fig. S6. Specifically, a silicon wafer was used as a substrate and was ultrasonically cleaned once with acetone and subsequently twice with ethanol. After drying the silicon wafer, 20 μL of 2.75×10^{-5} M Nile red solution was dropped onto it. After drying again, 10 μL of superparticle solution was dropped on it. Once dry, the wafer was covered with a copper mesh with a scale. The superparticles for testing were first confirmed under a scanning electron microscope and then tested with the Raman detection equipment. A $50\times$ objective was used, and the laser spot size was about 1 μm , and 150 g/mm grating. Typically, 1% of the laser power, a 10-s integration time, and 1 integration were used in the SERS measurements.

The equipment and wafer cleaning procedures for R6G Raman testing are the same as described above. The cleaning procedure for the test equipment and wafers is the same as above. Afterwards, 20 μL of 1×10^{-5} M R6G solution was added to the clean silicon wafer, waited for the wafer to dry, and then added the super particle solution again, and the silicon wafer was dried again and ready for testing.

FDTD simulations

The electric field simulations of superparticle regions were conducted using the finite-difference-time-domain (FDTD) method. The FDTD simulations were performed using a software package from FDTD Solutions (Lumerical Solutions, Inc.). A total-field scattered-field (TFSF) was used as the light source to simulate the interaction between a plane light wave and GNRs, with the light wavelength set to be 633 nm. The dimensions of the GNRs were set based on the average values obtained from experimental measurements. Within the boundary, the GNRs and the surrounding medium were divided into 1-nm grids. The gap between the GNRs is set according

to the actual situation, and the refractive index of the surrounding medium was set to be 1.33 (water).

Characterizations

All absorption measurements were captured on a UV-1900i spectrophotometer (SHIMADZU, Japan) with a 10-mm optical path, whereby a glass cuvette filled with Milli-Q water or toluene was used as the reference. Transmission electron microscopy (TEM) images were captured on a HT-7700 microscope (HITACHI, Japan) operating at 100.0 kV. Energy disperse spectroscopy (EDS) mapping were performed by a Fei-Talos-F200S operated at 200 kV. Scanning electron microscopy (SEM) images were captured using Sigma 500 operating at 3 kV. The SERS test was conducted using a LabRAM HR Evolution instrument with a laser wavelength of 633 nm and a laser power of 1%. The microscope images were captured using the built-in optical microscope of the Raman equipment with a $50\times$ objective lens.

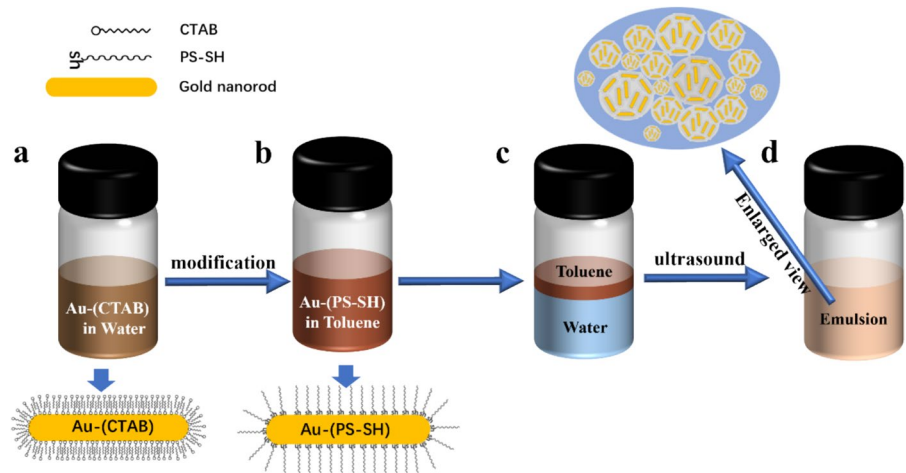
Results and discussion

In this study, we surface-modified two types of GNRs with different aspect ratios and then used the emulsion evaporation self-assembly method to form superparticles with SERS effects. The specific steps are shown in Fig. 1. Figure 1a shows the GNRs during synthesis, where the surface of the GNRs was coated with CTAB and dispersed in water. Figure 1b shows the GNRs after being modified with PS-SH, enabling them to be well-dispersed in toluene. In Fig. 1c, the toluene solution of the modified GNRs was concentrated and mixed with water. Due to the oleophilic nature of the GNRs, a clear phase separation could be observed. After sonication, the toluene formed small droplets and created an emulsion, as shown in Fig. 1d. Following evaporation, the GNRs aggregate and eventually formed superparticles. We then conducted a series of tests on the SERS performances of these superparticles and performed corresponding FDTD simulations on these nanostructures.

GNRs synthesis, purification, and modification

To explore the properties of superparticles formed by the self-assembly of GNRs with different aspect

Fig. 1 Schematic diagram of the superparticle synthesis. **a** Initially synthesized gold nanorods (dispersed in water); **b** PS-SH modified gold nanorods (dispersed in toluene); **c** Au-(PS-SH) toluene solution mixed with a certain amount of SDS and dextran (before sonication); **d** water emulsion formed after sonication and its partial magnified view. For ease of understanding, the molecular sizes in the diagram are not drawn to actual scale



ratios, we synthesized two types of GNRs with different aspect ratios. The TEM images and spectra of the GNRs are shown in Fig. 2a and b. We measured

the dimensions of ~150 GNRs using TEM images, finding that the average length of the GNRs in Fig. 2a is 113 ± 12.9 nm with an average diameter of

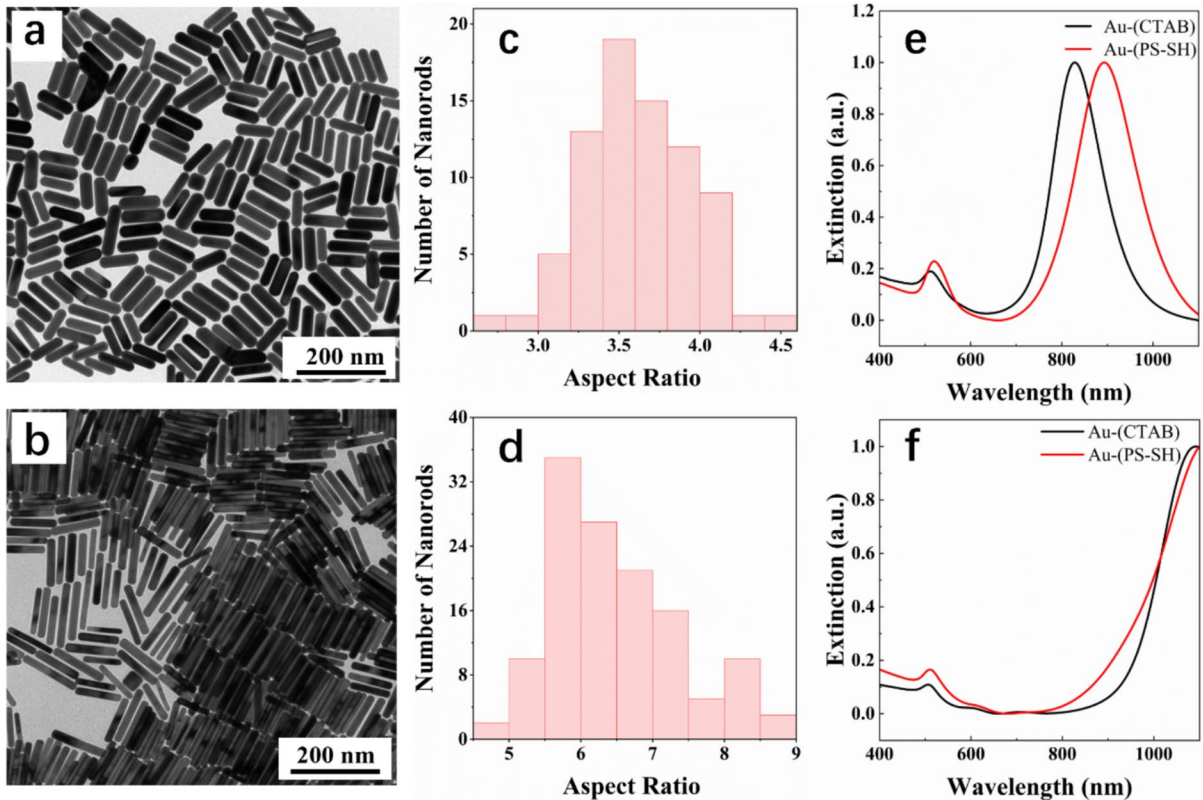


Fig. 2 Extinction spectra and TEM characterization of gold nanorods. **a** TEM image of lo-GNRs; **b** TEM image of hi-GNRs; **c** aspect ratio distribution of lo-GNRs; **d** aspect ratio distribution of hi-GNRs; **e** spectra of hi-GNRs before (Au-

(CTAB)) and after (Au-(PS-SH)) modification with PS-SH; **f** spectra of hi-GNRs before (Au-(CTAB)) and after (Au-(PS-SH)) modification with PS-SH

31.1 ± 5.0 nm, and the average length of the GNRs in Fig. 2b is 109.1 ± 12.7 nm with an average diameter of 17.0 ± 2.3 nm. It is evident that the average length difference between the two types of GNRs is only 4 nm, but the diameter difference is 14 nm, resulting in significantly different aspect ratios. The aspect ratio of the GNRs in Fig. 2a is about 3.5, which we refer to as low aspect ratio GNRs (lo-GNRs), while the aspect ratio of the GNRs in Fig. 2b is about 6.0, referred to as high aspect ratio GNRs (hi-GNRs).

We used a lower pH for the synthesis of hi-GNRs, which reduces the reaction rate and makes it easier to form gold nanorods with high aspect ratios, but after synthesis we found that many impurities were generated (such as gold nanospheres and gold nanocubes) [46–48]. Therefore, purification was necessary before the self-assembly of GNRs. We added an excess amount of CTAB to the synthesized gold nanorod solution, which induces the larger GNRs to precipitate preferentially, while the smaller by-products remain in the supernatant. After removing the supernatant, the purified GNRs are obtained. The spectra before and after purification were shown in Fig. S1. The spectra indicated that the absorption peaks at 500 nm and 560 nm, corresponding to gold nanospheres and gold nanoplatelets, respectively, were significantly reduced after purification [49]. The comparison of the actual solutions in Fig. S1b also showed that the color of the gold nanorod solution changed from purple-red to brown after purification.

When conducting SERS tests, the binding degree between the substrate and the dye was crucial. Initially, synthesized GNRs were modified with CTAB, which is hydrophilic, allowing for tight binding with water-soluble dyes. However, the binding affinity of GNRs to hydrophobic dyes was not as good. Additionally, GNRs typically required surface modification before self-assembly because they were inherently unstable and tend to aggregate, especially in organic solvents [50].

To expand the application range of GNRs and increase their stability, we used PS-SH to modify the surface of the GNRs. After modification with PS-SH, the GNRs can remain dispersed in toluene for extended periods. During self-assembly, because PS-SH is a macromolecule, the distance between GNRs can be easily adjusted by regulating the molecular weight of PS-SH. By controlling the molecular weight of PS-SH, the outcome of the self-assembly

process can be effectively tuned [51]. The shorter the distance between the GNRs, the stronger the coupling effect. To achieve a stronger coupling effect, PS-SH with a molecular weight of 5 k was used for surface modification.

The sulfhydryl group's binding to GNRs is much stronger than that of CTAB, allowing PS-SH to easily replace CTAB on the surface of the GNRs in THF solution [51, 52]. However, since the replacement process took time, 200 μ L of water was left in the solution when adding the GNRs to the PS-SH solution, enhancing the stability of the GNRs. Continuous sonication was used during the replacement process to prevent agglomeration until the PS-SH modification was successful. We refer to the CTAB-coated GNRs as Au-(CTAB), and the PS-SH-modified GNRs as Au-(PS-SH). The solution spectra of GNRs before and after surface modification are shown in Fig. 2c (lo-GNRs) and Fig. 2f (hi-GNRs). Note that the spectra of Au-(CTAB) were detected in an aqueous solution, while the spectra of Au-(PS-SH) were detected in toluene. Taking lo-GNRs as an example, one can see from the spectra that the absorption peak wavelength of Au-(PS-SH) was 893 nm, while that of Au-(CTAB) is 828 nm, indicating a redshift of 65 nm. This shift was mainly due to the change in the refractive index of the medium around the GNRs after replacing CTAB with PS-SH. The refractive index is related to the optical dielectric constant of the external medium (solvent, surfactant, carrier).

Additionally, the half-height width of the absorption peaks of the Au-(PS-SH) spectra remained almost unchanged, indicating that the modified GNRs were stably dispersed in toluene without agglomeration. To further prove that PS-SH successfully replaced CTAB, we dispersed the PS-SH-modified GNRs in toluene and mixed them with water. As shown in Fig. S2a and S2b, the dark liquid is Au-(PS-SH), and the colorless liquid is water. The clear phase separation of the two liquid layers indicates that the surface modification was successful, changing the hydrophilicity of the GNRs to lipophilicity. The HAADF-STEM images as well as EDS mapping of the gold nanorods are shown in Figure S3. Since the surface of the PS-SH-modified gold nanorods contains sulfur element, it is intuitively obvious that PS-SH has been successfully modified on the surface of the gold nanorods by observing the distribution of Au and sulfur.

Self-assembly of GNRs-(PS-SH)

An emulsion volatilization self-assembly method was employed to form superparticles from GNRs. After surface modification with PS-SH, the GNRs became lipophilic and could be well dispersed in toluene. First, the Au-(PS-SH) particles were dispersed in toluene and then mixed with an aqueous solution, followed by sonication to form an oil-in-water emulsion. A certain amount of SDS with dextran was added to the aqueous solution to facilitate better emulsion formation. After 2 min of sonication, the toluene turned into small droplets. The mixture was then left to stand for 3 days, during which the strong volatility of toluene caused it to evaporate gradually, bringing the GNRs in the toluene droplets closer together until the toluene was completely volatilized, and the particles stabilized.

Due to the uneven size of the toluene droplets obtained by ultrasonication, the sizes of the resulting superparticles were quite polydisperse, ranging from several hundred nanometers to a few micrometers (microscope images of the emulsion are shown in Fig. S4). Although this self-assembly method might result in some dispersed GNRs, most of them could be removed in subsequent low-speed centrifugation (2500 rpm). The final product derived from lo-GNRs was shown in Fig. 3a. After self-assembly, the GNRs were tightly bound together, forming stable superparticles that could be stored in aqueous solution for a long time (the particles in the figure were photographed after being stored for two months). Figure 3b shows the size distribution of the superparticles, with statistical data sourced from Fig. 3a. Although the overall size was relatively small, mostly distributed between 200 and 300 nm, there are also many larger particles (up to 10 μm). As a result of the extensive aggregation of GNRs into superparticles, their properties changed significantly. As shown in Fig. 3c, compared to the gold nanorod solution, the absorption peak wavelength of the superparticle solution shifts to blue (from 893 to 793 nm). This was mainly because the GNRs were primarily bounded in a shoulder-to-shoulder configuration, which effectively reduced their aspect ratio, leading to the blue shift of the absorption peak. Additionally, due to the varying sizes of the superparticles and their widespread dispersion in the solution, the absorption peak of the superparticle aqueous solution broadened, with high

absorption across wavelengths from 500 to 1100 nm. This indicated that superparticles could be suitable for a wider range of environments.

Figure 3d shows the SEM image of the superparticles formed by the self-assembly of hi-GNRs. Figure 3e presents the size distribution of the superparticles, with statistical data sourced from Fig. 3d. The sizes of the superparticles were mainly distributed between 400 and 500 nm. Figure 3f shows the spectrum of their aqueous solution, where a similar blue shift and broadening of the absorption peak are observed, for the same reasons mentioned earlier.

Superparticles with size-dependent SERS performances

To investigate the SERS performances of superparticles with different sizes and morphologies, we conducted localized testing of the superparticles. Given that the GNRs were modified with PS-SH, they can bind more tightly with Nile red, whereas other hydrophilic dyes such as 4-MBA and methylene blue have difficulty binding. Fig. S5 shows the Raman spectra of three dyes after passing through the superparticles following the same procedure. The differences were quite significant. Therefore, we chose Nile red as the dye for testing.

The specific procedure of SERS test involved first applying a drop of Nile red dye onto a clean silicon wafer and allowing it to dry. Subsequently, a drop of the superparticles aqueous solution was added to the silicon wafer and dried again. Finally, a copper grid with scales was placed over the dried sample. The superparticles to be tested were first observed under a scanning electron microscope (SEM), and their positions were recorded. Next, the copper mesh scale was observed under low magnification and recorded. Finally, the same point was located on the SERS test instrument using a microscope for testing. The specific steps were shown in Fig. S6a. Fig. S6b is the SEM image of the superparticle to be tested under the electron microscope, Fig. S6c was the SEM image of the copper mesh under low magnification, and Fig. S6d was the image observed under the optical microscope during the actual test. The scale and the special pattern in the middle of the copper mesh allowed us to determine the position of the particles to be tested.

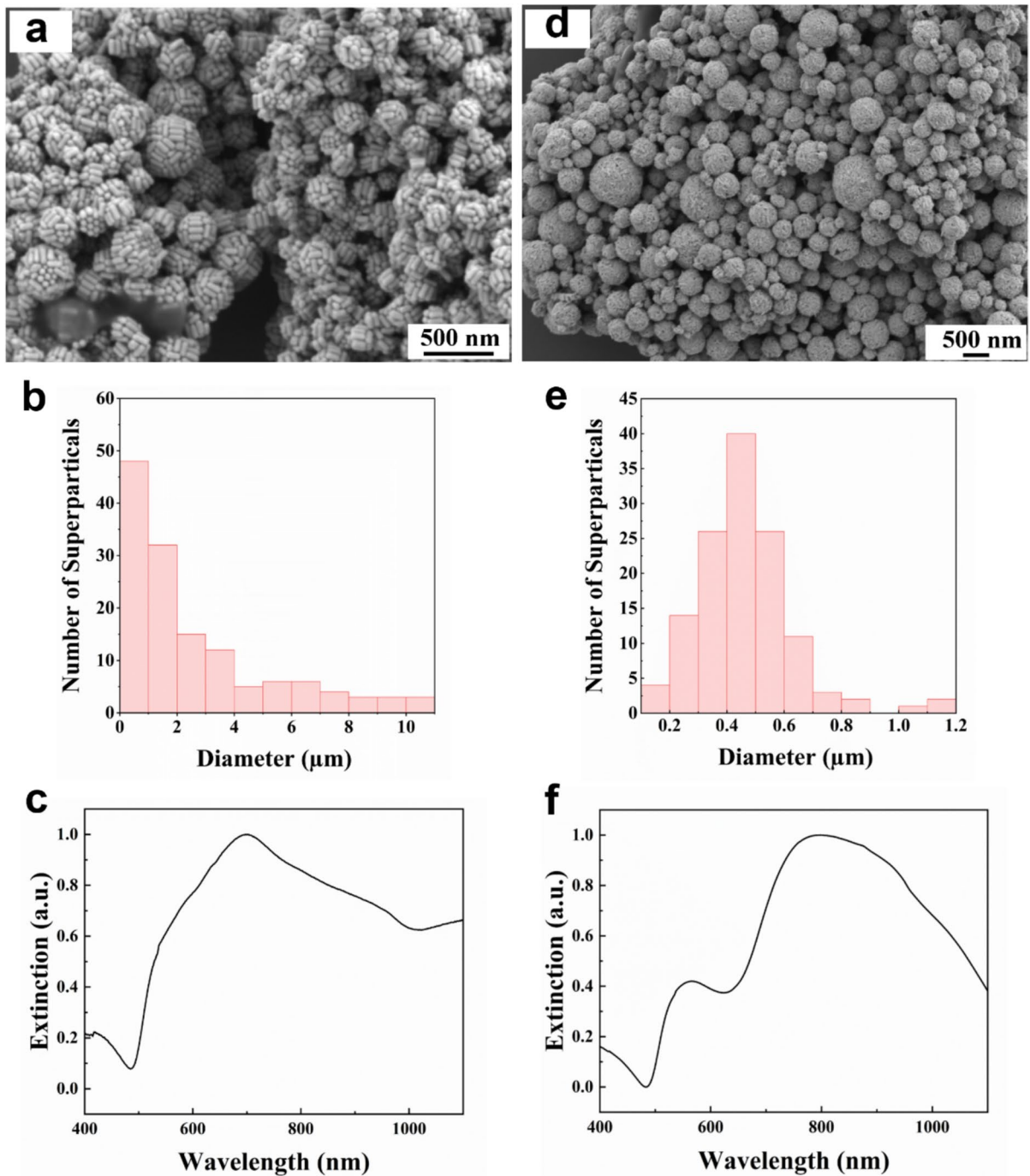


Fig. 3 Extinction spectra and SEM characterization of the gold nanorod superparticles. **a,b** SEM image (**a**) and size distribution (**b**) of the superparticles composed of lo-GNRs. **c** Extinction spectrum of aqueous solution of superparticles

composed of lo-GNRs. **d,e** SEM image (**d**) and size distribution (**e**) of superparticles composed of hi-GNRs. **f** Extinction spectrum of aqueous solution of superparticles composed of hi-GNRs

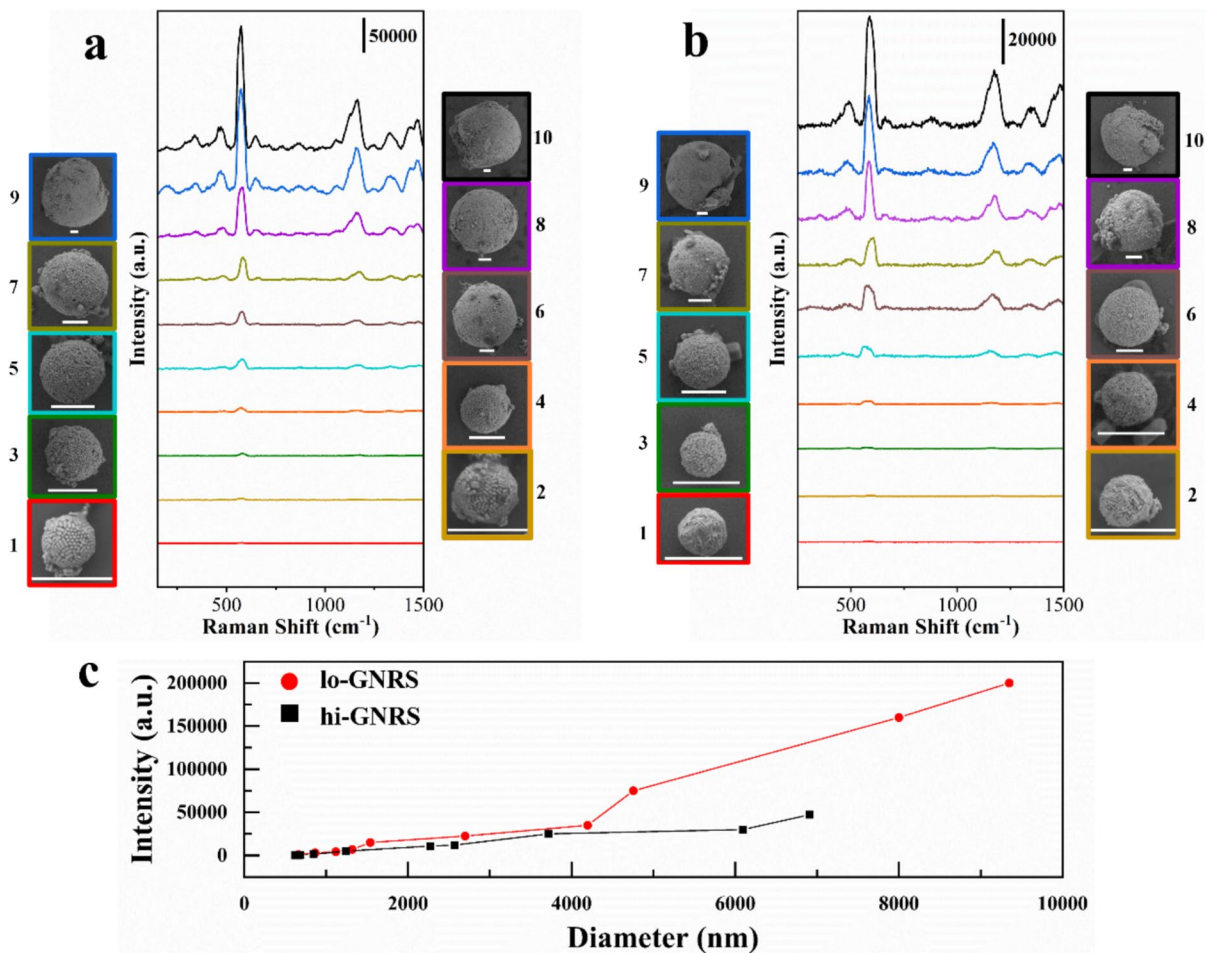


Fig. 4 SERS tests of superparticles and the corresponding SEM characterization. **a** Superparticles testing composed of lo-GNRs. The size of the superparticles gradually increased from 1 to 10 μm , and the color of the Raman signal curves corresponds to the color of the borders of the SEM images of the superparticles. **b** Superparticle testing composed of hi-GNRs.

First, we selected ten superparticles composed of lo-GNRs for testing. The SEM images of the ten superparticles correspond to Fig. 4a(1)–4a(10), with corresponding diameters ranging from 0.66 to 9.35 μm . The Raman spectra corresponding to the superparticles were shown in the middle of Fig. 4a, with a one-to-one correspondence between the superparticles and the spectrograms indicated by color. The excitation wavelength used was 633 nm. The peaks at 590 nm in the figure were the characteristic peaks of Nile red dye, and the peaks at 500 nm were the characteristic peaks from the silicon wafer. By comparison, we found that the intensity of the characteristic

The size of the superparticles gradually increases from 1 to 7 μm . **c** The relationship between particle size and Raman signal intensity for particles in Fig. 4a (red) and Fig. 4b (black). Nile red was used for SERS testing, with the Raman characteristic peak at 589 cm^{-1} . All scale bars in the SEM images are 1 μm

peaks of Nile red dye gradually increased with the size of the superparticles. When the diameter of the superparticles was 0.66 μm , the intensity was only 1090, but when the diameter was 9.35 μm , the intensity exceeded 200,000, an enhancement of 183 times. We also examined the intensity of eight additional superparticles with diameters between 0.66 and 9.35 μm . We have entered more specific values in Table S1. We observed that the intensity of the Nile red characteristic peaks increased with increasing diameter. This was mainly because, as the diameter of the superparticles increased, more Nile red molecules could interact with their surfaces. Additionally, the

increase in volume was accompanied by an increase in the number of SERS hotspots, greatly enhancing the Raman signal intensity.

Correspondingly, we performed similar tests on hi-GNRs superparticles using the same methodology and concentration of Nile red. Again, ten superparticles were selected, with diameters gradually increasing from 0.62 to 6.91 μm . The corresponding SEM images are shown in Fig. 4b(1)–b(10). In the middle of Fig. 4b are the Raman spectra of the superparticles, with a color correspondence between the superparticles and the spectra. The same pattern was observed: as the size of the superparticles increased, the intensity of the characteristic peaks of Nile red dye gradually increased. When the diameter of the superparticles was 0.62 μm , the intensity was only 160, but when the diameter was 6.91 μm , the intensity exceeded 47,250, an enhancement of 295 times. We have compiled the sizes of all superparticles and recorded them in detail in Table S2.

Figure 4c illustrated the relationship between the diameter of the two types of superparticles and their Raman signal intensity. It was evident that as the size of the superparticles increased, the Raman signal intensity also increased. Additionally, by comparing superparticles composed of different GNRs, it could be observed that when the sizes were similar, the Raman signal of superparticles made from lo-GNRs is significantly stronger than that of those made from hi-GNRs. In Fig. 4a(1), the superparticle has a diameter of 0.66 μm , corresponding to a Nile red Raman signal intensity of 1090, while in Fig. 4b(3), the superparticle has a diameter of 0.68 μm , with a corresponding Nile red Raman signal intensity of 525. Despite the close size of the two superparticles, the Nile red Raman signal intensity differed by nearly a factor of two. To make it easier to observe the surface morphology of the superparticles, we provide magnified images, as shown in Fig. S7 and Fig. S8.

We hypothesized that these intensity differences were primarily due to the different diameters of the GNRs composing the superparticles. As mentioned earlier, we used two types of GNRs for self-assembly: hi-GNRs with a diameter of 17 nm and lo-GNRs with a diameter of 31.1 nm. Despite a small difference in length (only 4 nm), the significant difference in diameter led to distinct properties of the resulted superparticles. According to our experimental findings, larger diameter GNRs, when length

was held constant, resulting in superparticles with superior SERS performances.

The electric field strength of individual particles is highly dependent on the morphology, and the presence of sharp regions usually produces a higher electric field [9]. In the case of gold nanorods, which are both used in this paper, the difference in morphology between the two gold nanorods is very small, but a larger volume of gold nanorods usually results in a stronger electric field [53]. At the same time, we simulated the electric field strength at single particles of the two gold nanorods in the paper using FDTD. As shown in Fig. S9, Fig. S9a is lo-GNRs with the highest electric field strength of 31, and Fig. S9b is hi-GNRs with the highest electric field strength of only 25. However, in the formation of superparticles, smaller constituent particles required more particles to achieve the same volume, potentially increasing the number of hotspots through coupling effects. Nevertheless, particles with larger diameters, which inherently possessed stronger electric fields, could generate more substantial electric fields when coupled together. While increasing the number of hotspots in superparticles was beneficial, the impact might be marginal due to existing numerous hotspots within the superparticles themselves. Thus, superparticles composed of lo-GNRs demonstrate stronger SERS performances due to their larger diameter, which enhanced their overall electric field strength and thus their SERS capability.

In addition, as we mentioned before, the reason for choosing 5 k molecular weight PS-SH is that smaller molecular weight PS-SH will result in smaller spacing between nanoparticles and thus better SERS performance. As a comparison we used PS-SH-11 k-modified gold nanorods to form super particles for SERS testing. As shown in Fig. S10, it can be found that although the Raman signal improves with the increase of the size of the superparticles, but it is limited, the largest particle is 1.2 μm , but the Raman signal intensity is only 1100, whereas the same size of superparticles modified by PS-SH-5 k reaches 4300 (The corresponding superparticles are Fig. 4a(3)). All three superparticles have weaker Raman signals than the corresponding size of superparticles modified by PS-SH-5 k. This proves that the SERS performances of the PS-SH-5 k-modified gold nanorods do perform better than of the PS-SH-11 k samples.

In order to further prove our conclusion, we also carried out the corresponding simulation experiments, as shown in Fig. S11, the pitch of the gold nanorods in S10a is 4 nm, and the pitch in S10b is 2 nm, and the highest electric field strength in S10a is 9.1, while the highest electric field strength in S10b is 21.5, the difference between the two is huge. This demonstrates that as the distance of the gold nanorods decreases, it is more favorable to generate stronger electric fields and thus better SERS performance.

To prove the universality of the superparticles, we added the Raman test of R6G dye molecules. Superparticles composed of lo-GNRs were used in this experiment. The main Raman characteristic peaks of R6G are at 1359 cm^{-1} and 1507 cm^{-1} . The green spectrum in Fig. S12 is tested without superparticles, and it can be found that the intensity is very low, and the intensity is greatly improved after the addition of superparticles, and the strongest signal can reach 7000. This proves that superparticles can be applied to a wider range of Raman detection.

FDTD simulations

To validate our conclusions, we also conducted FDTD simulations. Upon examining the structure of the superparticles, we observed that the local gold nanorods were arranged side by side in a very orderly manner (as shown in the magnified SEM image of the superparticles in Fig. S13). Therefore, we used ordered layer(s) in our simulations. A 633-nm laser was used for excitation in the simulations, to closely match the experimental conditions. For the polarization direction of the incident light, we selected two orientations: one perpendicular to the longitudinal axis of the gold nanorods and the other parallel to it. This was necessary because the orientation of the nanorods on the surface of the superparticles was not uniform in practice, requiring simulations in multiple directions.

The simulated results are shown in Fig. 5, where Fig. 5a–j displays the FDTD simulated electric field intensity when the polarization direction of the incident light was parallel to the longitudinal axis of the GNRs. The number of GNRs increased gradually from Fig. 5a–e, and as this number increased, the

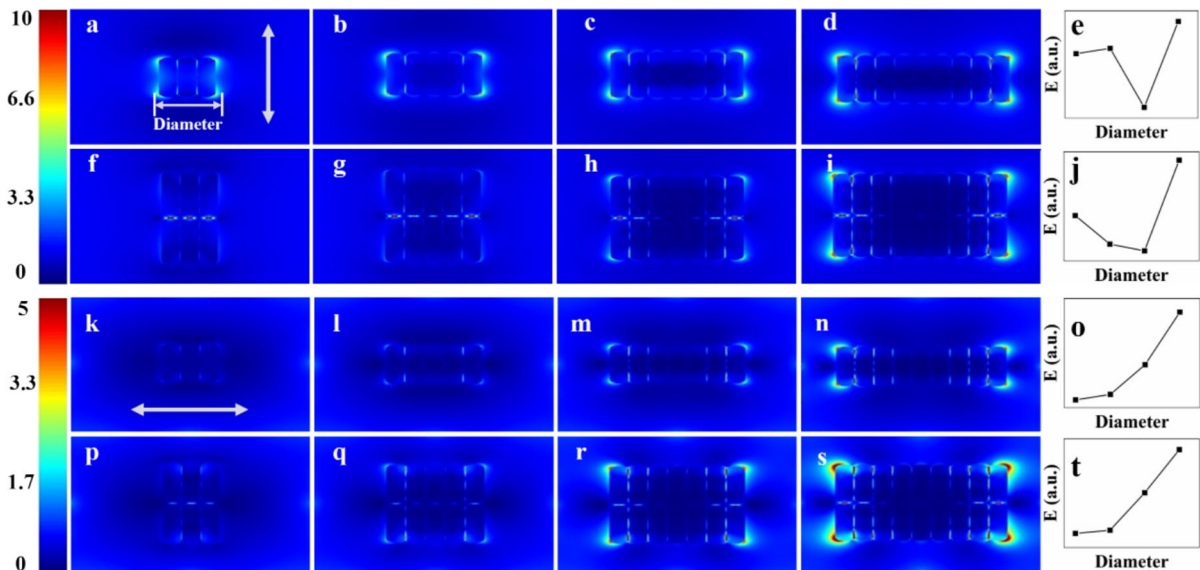


Fig. 5 FDTD simulations of the electric field intensity in specific regions of superparticles. **a, b, c, d** Increasing number of GNRs in a single layer. **e** Graph of the relationship between diameter and electric field intensity. **f, g, h, i** Increasing number of GNRs in two layers. **j** Graph of the relationship between diameter and electric field intensity. **k, l, m, n, o, p, q, r, s, t**

Same structures as (a, b, c, d, e, f, g, h, i, j) but with a different light polarization direction. In (a, b, c, d, e, f, g, h, i, j), the polarization direction of the light is parallel to the longitudinal axis of the gold nanorods, while in (k, l, m, n, o, p, q, r, s, t), the polarization direction is perpendicular to the longitudinal axis of the gold nanorods

diameter of the structure composed of GNRs also increased. Despite fluctuations in the electric field intensity, the overall intensity was enhanced with the increased diameter. The highest electric field intensity is 10.1 at a diameter of 96 nm in Fig. 5a and 13.3 at a diameter of 288 nm in Fig. 5d. The relationship between the electric field and the diameter of the gold nanorod structure is shown in Fig. 5e.

Figure 5f–j has an additional layer of GNRs compared to Fig. 5a–e, making the structure closer to that of the superparticles. As the number of GNRs increased in these figures, so did the diameter and the electric field intensity. For instance, Fig. 5f has a diameter of 96 nm with the highest intensity of 13.3, while Fig. 5i had a diameter of 288 nm with the highest intensity of 29.9. It was worth noting that although the structure in Fig. 5f had only one additional layer of GNRs compared to Fig. 5a, the electric field strength increased significantly from 1.96 to 3.68. The same pattern was observed for Fig. 5b vs. Figure 5g, Fig. 5c vs. Figure 5h, and Fig. 5d vs. Figure 5i.

Figure 5k–n showed the electric field strength of the FDTD simulation when the direction of incident light polarization was parallel to the longitudinal axis of the GNRs. In these figures, as the number of GNRs increased, the electric field strength raised from 1.96 to 10.4. The trend is illustrated in Fig. 5o. Figure 5p–s, which added a layer of GNRs, showed a similar increase in electric field strength from 3.68 to 14.4. The trend was shown in Fig. 5t.

Summarizing the above, we found that regardless of the polarization direction of the incident light, increasing the number of GNRs enhanced the electric field strength. However, if the number of GNRs was increased only in two dimensions, the electric field enhancement was limited. In contrast, a three-dimensional increase in the number of GNRs, such as adding a layer, results in a significant enhancement of the electric field strength. Since the superparticle itself was a three-dimensional structure, not a simple two-dimensional plane assembly, the electric field strength increased with the size of the superparticle, thereby improving SERS performances. This observation aligned closely with our experimental results, which were detailed in Table S3.

Additionally, we performed the same FDTD simulations for the structures composed of hi-GNRs, as shown in Fig. S14. To closely match

the experiments, the overall size of the simulated structures in Fig. S14a–S14t and Fig. 5a–t were similar, with a diameter difference of less than 20 nm and the same height. Apart from the size similarity, other simulation conditions were identical, except that the smaller diameter of the GNRs in Fig. S14 resulted in more nanorods. After comparison, we found that the highest E-field intensity of Fig. S14a–S14t is 14.5, whereas for Fig. 5a–t it is 29.5. This result was consistent with our experiments, demonstrating that structures formed by hi-GNRs had stronger SERS performances than those formed by lo-GNRs. Detailed values are recorded in Table S4.

Conclusion

In summary, we synthesized two types of gold nanorods with different aspect ratios. By modifying them with PS-SH and employing an emulsion evaporation self-assembly method, we successfully formed superparticles with strong SERS performance. Our investigations revealed that the SERS performances of these superparticles improved with increasing size. This enhancement can be attributed to the larger surface area available for dye molecule interaction as well as the increased volume that creates more SERS hotspots, thereby amplifying Raman signal intensity. Specifically, when superparticles are of the same size, those composed of larger-diameter GNRs exhibit superior SERS performances due to their larger volume, which generates a stronger electric field upon coupling. To substantiate our findings, FDTD simulations were conducted based on a shoulder-to-shoulder arrangement of GNRs within the superparticles. These simulated results demonstrated that as the size and number of GNRs in the simulated assemblies increased, the electric field strength and number of SERS hotspots also increased. At the same time, the maximum electric field strength of the larger diameter gold nanorods is greater than that of the smaller diameter gold nanorods, aligning well with our experimental observations. The self-assembly method employed here is straightforward and effective, yielding superparticles with diverse size distributions and robust SERS capabilities. These attributes underscore its potential for various SERS substrate applications.

Acknowledgements The authors thank Sudan Shen for her assistance in TEM at State Key Laboratory of Chemical Engineering (Zhejiang University).

Author contribution G-LW: Investigation; Writing – original draft; Visualization. T-SD: Writing – review & editing; Funding acquisition; Supervision. K-PW: Investigation. E-JZ: Investigation. L-YL: Investigation. Y-CC: Investigation. J-FG: Investigation. JL: Writing – review & editing; Resources.

Funding T. S. Deng acknowledge financial support from Zhejiang Provincial Natural Science Foundation (Grant: LY24F050008), Zhejiang Provincial Educational Ministry Scientific Research Project (Grant: Y202352284), and National Natural Science Foundation of China (NSFC, Grant: 61905056). This work was also supported by the Fundamental Research Funds for the Provincial Universities of Zhejiang (GK239909299001-301).

Data availability No datasets were generated or analysed during the current study.

Declarations

Conflict of interest The authors declare no competing interests.

References

1. Ma C, Trujillo MJ, Camden JP (2016) Nanoporous silver film fabricated by oxygen plasma: a facile approach for SERS substrates. *ACS Appl Mater Interfaces* 8:23978–23984. <https://doi.org/10.1021/acsami.6b08191>
2. Papadopoulou E, Bell SEJ (2011) Label-free detection of single-base mismatches in DNA by surface-enhanced Raman spectroscopy. *Angewandte Chemie-International Edition* 50:9058–9061. <https://doi.org/10.1002/anie.201102776>
3. Yang N, You T-T, Gao Y-K et al (2018) Fabrication of a flexible gold nanorod polymer metafilm via a phase transfer method as a SERS substrate for detecting food contaminants. *J Agric Food Chem* 66:6889–6896. <https://doi.org/10.1021/acs.jafc.8b01702>
4. Wu L, Wang Z, Zong S et al (2012) A SERS-based immunoassay with highly increased sensitivity using gold/silver core-shell nanorods. *Biosens Bioelectron* 38:94–99. <https://doi.org/10.1016/j.bios.2012.05.005>
5. Moldovan R, Toma V, Iacob B-C et al (2022) Off-resonance gold nanobone films at liquid interface for SERS applications. *Sensors* 22:236. <https://doi.org/10.3390/s22010236>
6. Peng X, Li D, Li Y et al (2021) Plasmonic tunable Ag-coated gold nanorod arrays as reusable SERS substrates for multiplexed antibiotics detection. *J Mater Chem B* 9:1123–1130. <https://doi.org/10.1039/d0tb02540b>
7. Zhang C, Huang L, Sun D-W et al (2022) Interfacing metal-polyphenolic networks upon photothermal gold nanorods for triplex-evolved biocompatible bactericidal activity. *J Hazard Mater* 426:127824. <https://doi.org/10.1016/j.jhazmat.2021.127824>
8. Chen HJ, Shao L, Li Q et al (2013) Gold nanorods and their plasmonic properties. *Chem Soc Rev* 42:2679–2724. <https://doi.org/10.1039/c2cs35367a>
9. Ding SY, Yi J, Li JF et al (2016) Nanostructure-based plasmon-enhanced Raman spectroscopy for surface analysis of materials. *Nat Rev Mater* 1:1–16. <https://doi.org/10.1038/natrevmats.2016.21>
10. Gabudean AM, Biro D, Astilean S (2011) Localized surface plasmon resonance (LSPR) and surface-enhanced Raman scattering (SERS) studies of 4-aminothiophenol adsorption on gold nanorods. *J Mol Struct* 993:420–424. <https://doi.org/10.1016/j.molstruc.2010.11.045>
11. Li JJ, Li T, Zhu J et al (2018) Reversible tuning the aspect ratio and plasmonic shift of gold nanorods in alkaline environment: growth, etching and rebuilding. *Plasmonics* 13:1433–1439. <https://doi.org/10.1007/s11468-017-0648-4>
12. Sánchez-Iglesias A, Winckelmans N, Altantzis T et al (2017) High-yield seeded growth of monodisperse pentatwinned gold nanoparticles through thermally induced seed twinning. *J Am Chem Soc* 139:107–110. <https://doi.org/10.1021/jacs.6b12143>
13. Meng LQ, Li ZX, Deng YS (2021) Study on the growth kinetics of Au nanorods based on local surface plasmon resonance. *Gold Bulletin* 54:89–95. <https://doi.org/10.1007/s13404-021-00299-0>
14. Gao Q, Qian Y, Xia Y et al (2011) A novel method to prepare high-aspect ratio gold nanorods. *Acta Chim Sinica* 69:1617–1621
15. Fernández-López C, Polavarapu L, Solís DM et al (2015) Gold nanorod-pNIPAM hybrids with reversible plasmon coupling: synthesis, modeling, and SERS properties. *ACS Appl Mater Interfaces* 7:12530–12538. <https://doi.org/10.1021/am5087209>
16. Ferrier RC, Lee HS, Hore MJA et al (2014) Gold nanorod linking to control plasmonic properties in solution and polymer nanocomposites. *Langmuir* 30:1906–1914. <https://doi.org/10.1021/la404588w>
17. Funston AM, Novo C, Davis TJ et al (2009) Plasmon coupling of gold nanorods at short distances and in different geometries. *Nano Lett* 9:1651–1658. <https://doi.org/10.1021/nl900034v>
18. Pramod P, Thomas KG (2008) Plasmon coupling in dimers of Au nanorods. *Adv Mater* 20:4300–4305. <https://doi.org/10.1002/adma.200703057>
19. Liu YY, Zhang YX, Ding HL et al (2013) Self-assembly of noble metallic spherical aggregates from monodisperse nanoparticles: their synthesis and pronounced SERS and catalytic properties. *J Mater Chem A* 1:3362–3371. <https://doi.org/10.1039/c3ta00953j>
20. Qian J, Jiang L, Cai FH et al (2011) Fluorescence-surface enhanced Raman scattering co-functionalized gold nanorods as near-infrared probes for purely optical in vivo imaging. *Biomaterials* 32:1601–1610. <https://doi.org/10.1016/j.biomaterials.2010.10.058>
21. Li J, Wang W, Xie C et al (2020) Facile fabrication of three-dimensional AuNPs@ AgNR arrays for highly sensitive SERS detection of 2, 3, 7, 8-TCDD.

- J Mater Sci 55:7029–7038. <https://doi.org/10.1007/s10853-020-04490-0>
22. Cakes AJ, Vaz RP, Fantini C et al (2015) Highly sensitive and simple SERS substrate based on photochemically generated carbon nanotubes-gold nanorods hybrids. *J Colloid Interface Sci* 455:78–82. <https://doi.org/10.1016/j.jcis.2015.04.071>
 23. Mitamura K, Imae T (2009) Functionalization of gold nanorods toward their applications. *Plasmonics* 4:23–30. <https://doi.org/10.1007/s11468-008-9073-z>
 24. Strickland AD, Batt CA (2009) Detection of carbendazim by surface-enhanced Raman scattering using cyclodextrin inclusion complexes on gold nanorods. *Anal Chem* 81:2895–2903. <https://doi.org/10.1021/ac801626x>
 25. Lee Y, Jang J, Yoon J et al (2019) Phase transfer-driven rapid and complete ligand exchange for molecular assembly of phospholipid bilayers on aqueous gold nanocrystals. *Chem Commun* 55:3195–3198. <https://doi.org/10.1039/c8cc10037c>
 26. Lista M, Liu DZ, Mulvaney P (2014) Phase transfer of noble metal nanoparticles to organic solvents. *Langmuir* 30:1932–1938. <https://doi.org/10.1021/la404569h>
 27. Metzman JS, Khan AU, Magill BA et al (2019) Critical role of polystyrene layer on plasmonic silver nanoplates in organic photovoltaics. *ACS Appl Energy Mater* 2:2475–2485. <https://doi.org/10.1021/acsaem.8b01860>
 28. Woo YJ, Park KH, Park OO et al (2015) Dispersion control of Ag nanoparticles in bulk-heterojunction for efficient organic photovoltaic devices. *Org Electron* 16:118–125. <https://doi.org/10.1016/j.orgel.2014.10.043>
 29. Feng LL, Xuan ZW, Ma JB et al (2015) Preparation of gold nanorods with different aspect ratio and the optical response to solution refractive index. *J Exp Nanosci* 10:258–267. <https://doi.org/10.1080/17458080.2013.824619>
 30. Pellas V, Hu DV, Mazouzi Y et al (2020) Gold nanorods for LSPR biosensing: synthesis, coating by silica, and bioanalytical applications. *Biosensors-Basel* 10:146. <https://doi.org/10.3390/bios10100146>
 31. Zheng Y, Thai T, Reineck P et al (2013) DNA-directed self-assembly of core-satellite plasmonic nanostructures: a highly sensitive and reproducible near-IR SERS sensor. *Adv Func Mater* 23:1519–1526. <https://doi.org/10.1002/adfm.201202073>
 32. Lu W, Wang H, Zhang J et al (2015) Gold nanorods: synthesis, growth mechanism and purification. *Progress in Chemistry* 27:785–793. <https://doi.org/10.7536/pc150111>
 33. Park K, Koerner H, Vaia RA (2010) Depletion-induced shape and size selection of gold nanoparticles. *Nano Lett* 10:1433–1439. <https://doi.org/10.1021/nl100345u>
 34. Van Der Hoeven JES, Gurunaryanan H, Bransen M et al (2022) Silica-coated gold nanorod supraparticles: a tunable platform for surface enhanced Raman spectroscopy. *Adv Func Mater* 32:2200148. <https://doi.org/10.1002/adfm.202200148>
 35. Albarghouthi N, Macmillan P, Brosseau CL (2021) Optimization of gold nanorod arrays for surface enhanced Raman spectroscopy (SERS) detection of atrazine. *Analyst* 146:2037–2047. <https://doi.org/10.1039/d0an02215b>
 36. Chen SH, Huang P, Wang ZH et al (2013) Self-assembly of gold nanoparticles to silver microspheres as highly efficient 3D SERS substrates. *Nanoscale Res Lett* 8:1–7. <https://doi.org/10.1186/1556-276x-8-168>
 37. Zhang Q, Lee YH, Phang IY et al (2014) Hierarchical 3D SERS substrates fabricated by integrating photolithographic microstructures and self-assembly of silver nanoparticles. *Small* 10:2703–2711. <https://doi.org/10.1002/smll.201303773>
 38. Qiao XZ, Su BS, Liu C et al (2018) Selective surface enhanced Raman scattering for quantitative detection of lung cancer biomarkers in superparticle@MOF structure. *Adv Mater* 30:1702275. <https://doi.org/10.1002/adma.201702275>
 39. Wang XN, Xu SP, Li HB et al (2012) A three-dimensional surface-enhanced Raman scattering substrate: Au nanoparticle supramolecular self-assembly in anodic aluminum oxide template. *J Raman Spectrosc* 43:459–463. <https://doi.org/10.1002/jrs.3041>
 40. Liu R, Li S, Liu J-F (2017) Self-assembly of plasmonic nanostructures into superlattices for surface-enhanced Raman scattering applications. *Trac-Trends Anal Chem* 97:188–200. <https://doi.org/10.1016/j.trac.2017.09.003>
 41. Zheng J, Dai B, Liu J et al (2016) Hierarchical self-assembly of Cu₇Te₅ nanorods into superstructures with enhanced SERS performance. *ACS Appl Mater Interfaces* 8:35426–35434. <https://doi.org/10.1021/acsaami.6b11058>
 42. Li X, Chen X, Liu J et al (2023) Superparticles of gold nanorods with controllable bandwidth and spectral shape for lipophilic SERS. *Nanoscale* 15:12270–12279. <https://doi.org/10.1039/d3nr01883k>
 43. Ye X, Zheng C, Chen J et al (2013) Using binary surfactant mixtures to simultaneously improve the dimensional tunability and monodispersity in the seeded growth of gold nanorods. *Nano Lett* 13:765–771. <https://doi.org/10.1021/nl304478h>
 44. Yue X, Liu X, Yan N et al (2020) Hierarchical colloidosomes with a highly ordered and oriented arrangement of gold nanorods via confined assembly at the emulsion interface. *J Phys Chem C* 124:20458–20468. <https://doi.org/10.1021/acs.jpcc.0c06162>
 45. Mason T, Bibette J (1997) Shear rupturing of droplets in complex fluids. *Langmuir* 13:4600–4613. <https://doi.org/10.1021/la9700580>
 46. Wei Q, Ji J, Shen J (2008) PH controlled synthesis of high aspect-ratio gold nanorods. *J Nanosci Nanotechnol* 8:5708–5714. <https://doi.org/10.1166/jnn.2008.302>
 47. Van Der Hoeven JE, Deng T-S, Albrecht W et al (2021) Structural control over bimetallic core-shell nanorods for surface-enhanced Raman spectroscopy. *ACS Omega* 6:7034–7046. <https://doi.org/10.1021/acsomega.0c06321>
 48. Lughì V (2016) Surface energy and chemical potential at nanoscale. *Springer Netherlands* 3907–3917. https://doi.org/10.1007/978-94-017-9780-1_276
 49. Ge YJ, Chi C, Wu R et al (2012) Gold nanorods-based core-shell nanostructures: synthesis, characterization and optical properties. *Prog Chem* 24:776–783. <https://doi.org/10.1016/j.ccr.2005.01.030>
 50. Zhang S, Geryak R, Geldmeier J et al (2017) Synthesis, assembly, and applications of hybrid nanostructures for biosensing. *Chem Rev* 117:12942–13038. <https://doi.org/10.1021/acs.chemrev.7b00088>

51. Schulz F, Pavelka O, Lehmkuhler F et al (2020) Structural order in plasmonic superlattices. *Nat Commun* 11:3821. <https://doi.org/10.1038/s41467-020-17632-4>
52. Zhang M, Deng TS, Cheng Z (2023) Ethanol as a ‘catalyst’ for effective phase transfer and self-assembly of gold nanorods. *ChemistrySelect* 8:e202301065. <https://doi.org/10.1002/slct.202301065>
53. Zhang EJ, Deng TS, Chen Z et al (2024) Seed-mediated synthesis of gold nanobipyramids at low CTAB concentration using binary surfactants. *Part Part Syst Charact* 2400190. <https://doi.org/10.1002/ppsc.202400190>

Publisher’s Note Springer Nature remains neutral with regard to jurisdictional claims in published maps and institutional affiliations.

Springer Nature or its licensor (e.g. a society or other partner) holds exclusive rights to this article under a publishing agreement with the author(s) or other rightsholder(s); author self-archiving of the accepted manuscript version of this article is solely governed by the terms of such publishing agreement and applicable law.

Supporting information

Synthesis of lipophilic gold nanorod superparticles and their size-dependent SERS performances

Gui-Lin Wu¹, Tian-Song Deng^{1,*}, Kun-Peng Wang¹, Er-Ji Zhang¹, Li-Yong Liu¹, Yu-Chun
Cheng¹, Jia-Fei Gao¹, and Jie Liu¹

¹*School of Electronics and Information Engineering, Hangzhou Dianzi University, Hangzhou
310018, P. R. China*

* *Corresponding author. E-mail: dengts@pku.edu.cn*

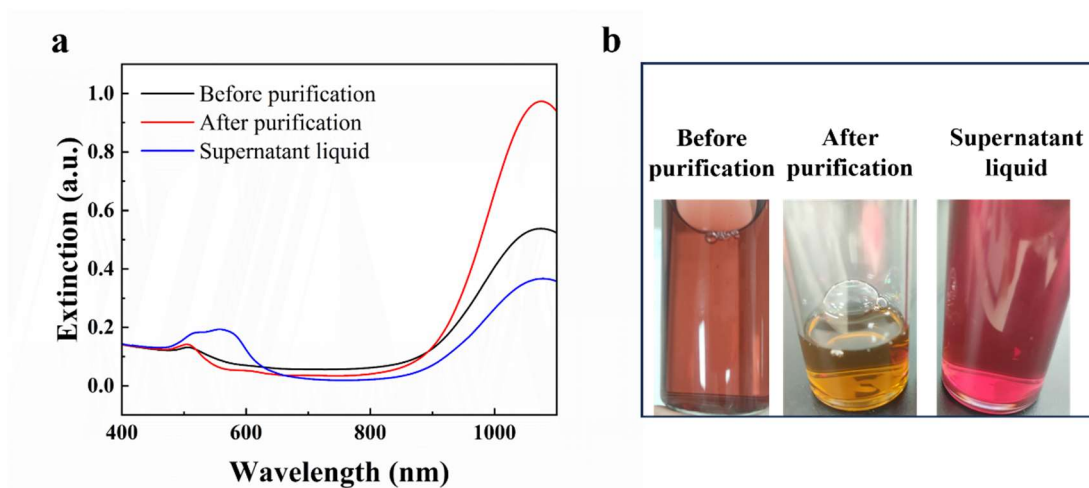


Figure S1 Extinction spectra characterization and physical comparison of gold nanorods before and after purification. (a) Extinction spectra of gold nanorods before purification (black), after purification (red), and the supernatant (blue). (b) Physical comparison of gold nanorods before purification, after purification, and the supernatant. The extinction peaks were both at 1074 nm for the spectra before and after purification.

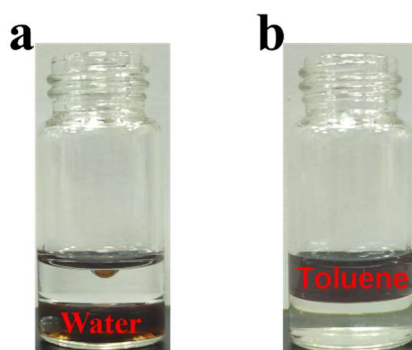


Figure S2 Comparison of Au-(CTAB) Aqueous Solution and Au-(PS-SH) Toluene Solution. (a) The upper layer is toluene, and the lower layer is the Au-(CTAB) aqueous solution. (b) The upper layer is the Au-(PS-SH) toluene solution. The distinct phase separation indicates that the surface modification of the gold nanorods was successful.

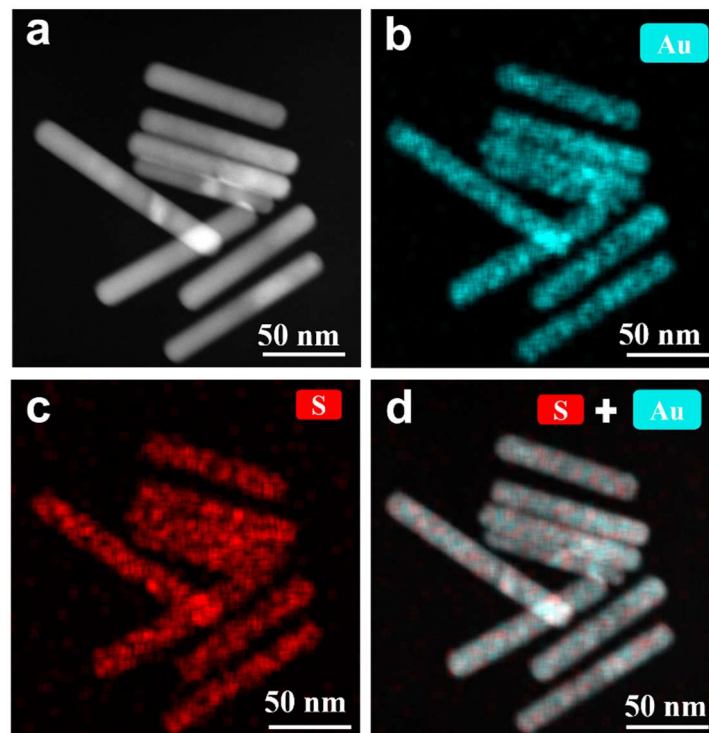


Figure S3 HAADF-STEM image and EDS mapping of PS-SH modified gold nanorods. (a) HAADF-STEM image (b) spatial distribution of Au (c) spatial distribution of S (d) spatial distribution of S and Au.

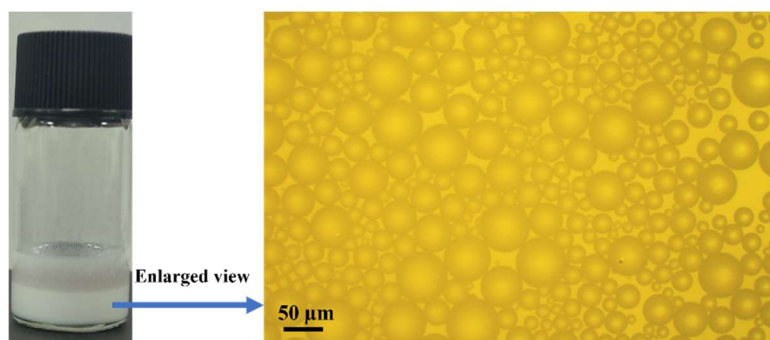


Figure S4 Microscope images of the water-in-toluene emulsions formed after ultrasonic mixing of toluene and water.

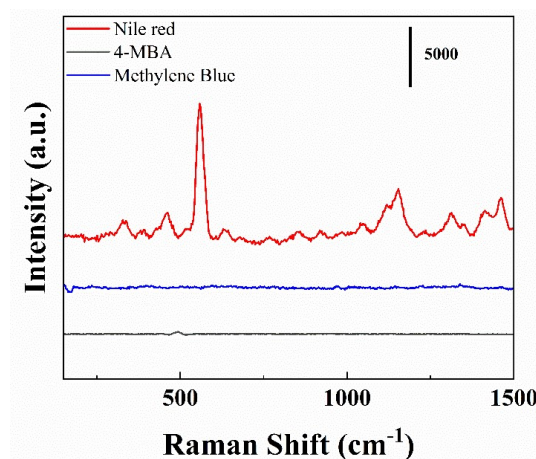


Figure S5 Comparison of SERS test results of superparticles using different dyes.

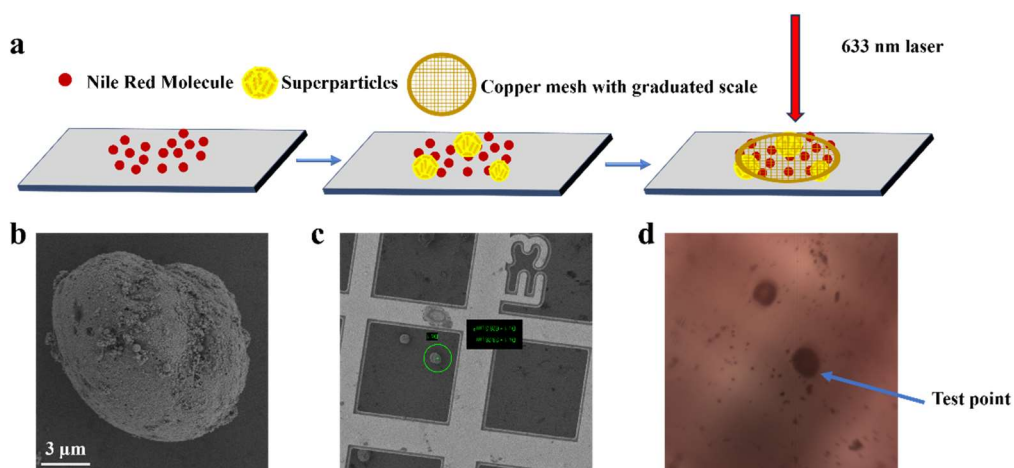


Figure S6 Localized SERS testing of superparticles. (a) Schematic illustration of the localized testing steps. First, Nile red dye is dropped onto a clean silicon wafer. After drying, a superparticle aqueous solution is added. After drying again, a copper grid with scales is placed on top for testing. (b) Scanning electron microscope (SEM) image of superparticles. (c) Magnified SEM image showing the copper grid scales clearly. (d) Optical microscope image taken during the actual testing.

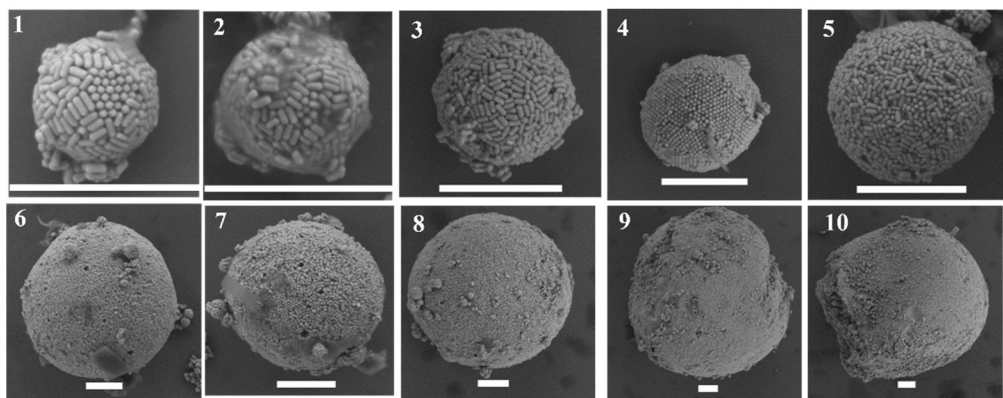


Figure S7 Enlarged images of the superparticles in Fig. 4a, corresponding to 4a1-4a10, respectively.

All scale bars in the SEM images are 1 μm .

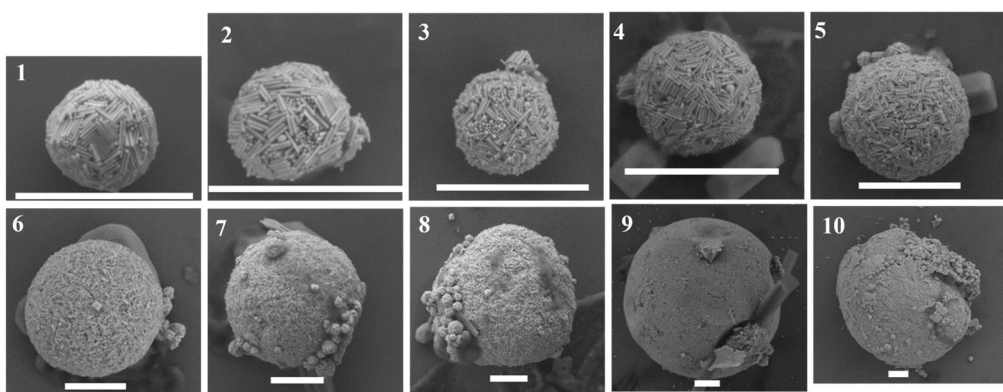


Figure S8 Enlarged images of the superparticles in Fig. 4b, corresponding to 4b1-4b10, respectively.

All scale bars in the SEM images are 1 μm .

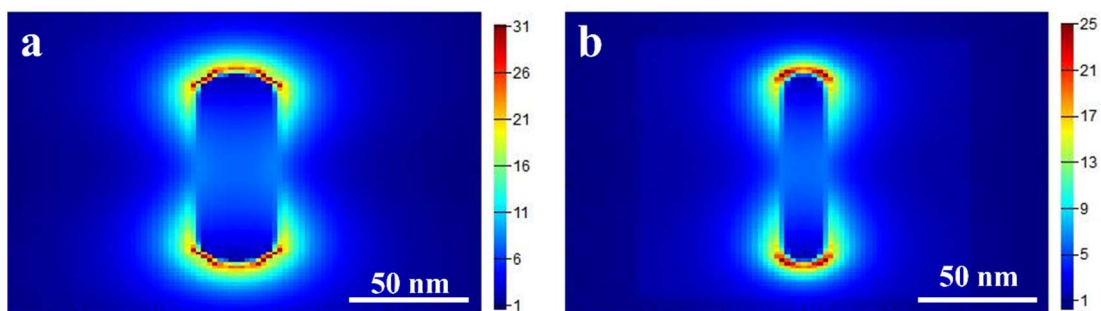


Figure S9 Single gold nanorod particle FDTD simulation. (a) lo-GNRs. (b) hi-GNRs.

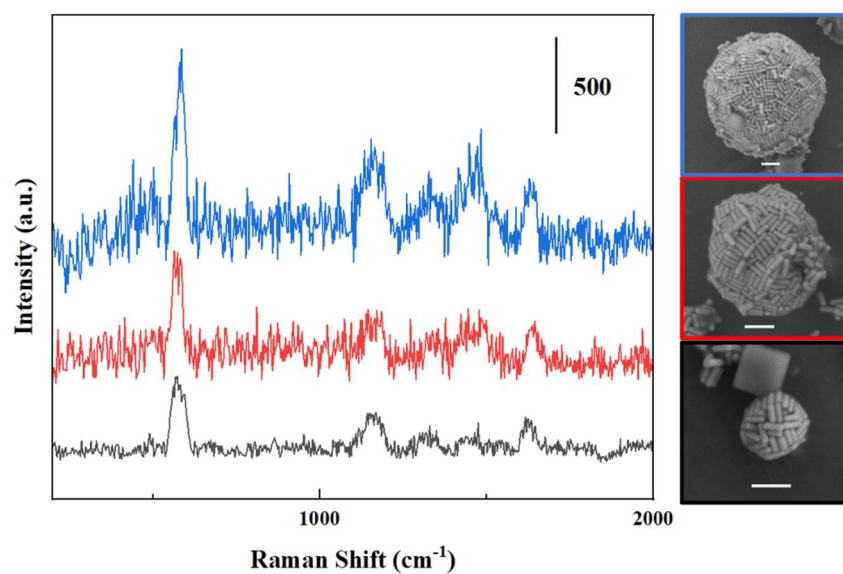


Figure S10 SERS test of superparticles assembled from gold nanorods modified with 11 k molecular weight of PS-SH (the dye used was Nile Red and all scale bars in the SEM images are 200 nm).

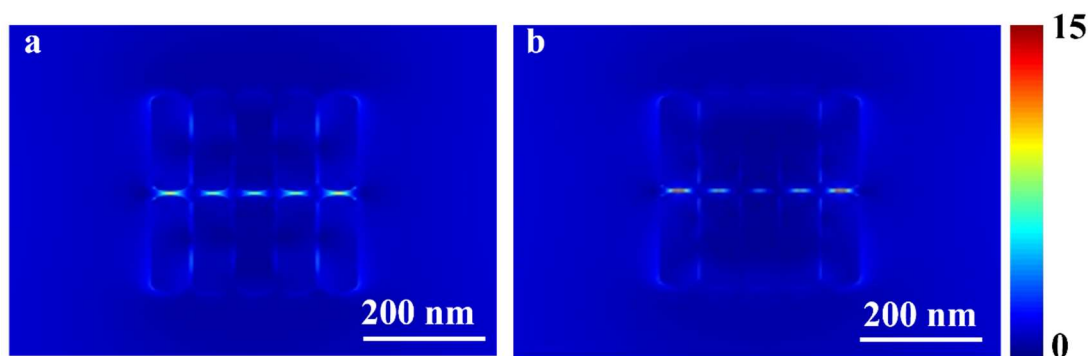


Figure S11 Comparison of the electric field strength of gold nanorods before and after increasing the spacing. (a) Electric field strength of gold nanorods at 4 nm spacing from each other. (b) E-field strength of gold nanorods with 2 nm spacing between them. The highest electric field strength is 9.1 in Fig. S10a and 21.5 in Fig. S10b.

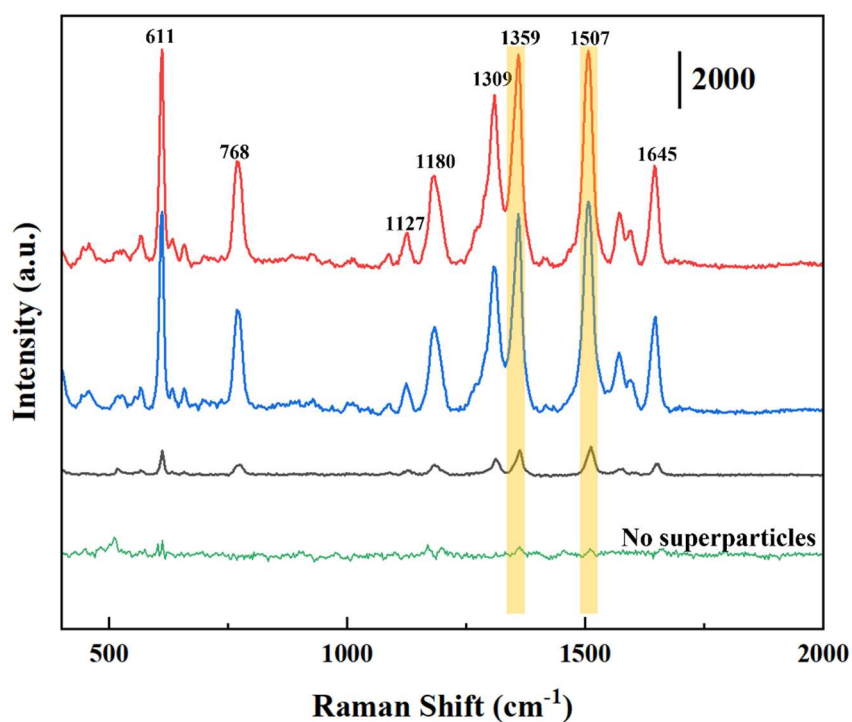


Figure S12 Raman test using R6G. Where the red, blue and black lines represent different super particles tested. The intensity is different because it is affected by the morphology of the superparticles. The green color is the data of the measurements performed when no superparticles were present.

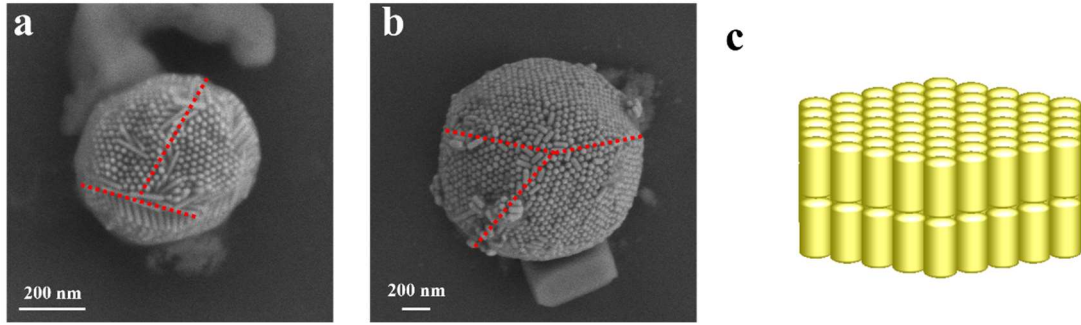


Figure S13 SEM images of superparticles and simulation structures. The image reveals many regions with gold nanorod arrays. This observed structure was used as the basis for designing the FDTD simulation structure.

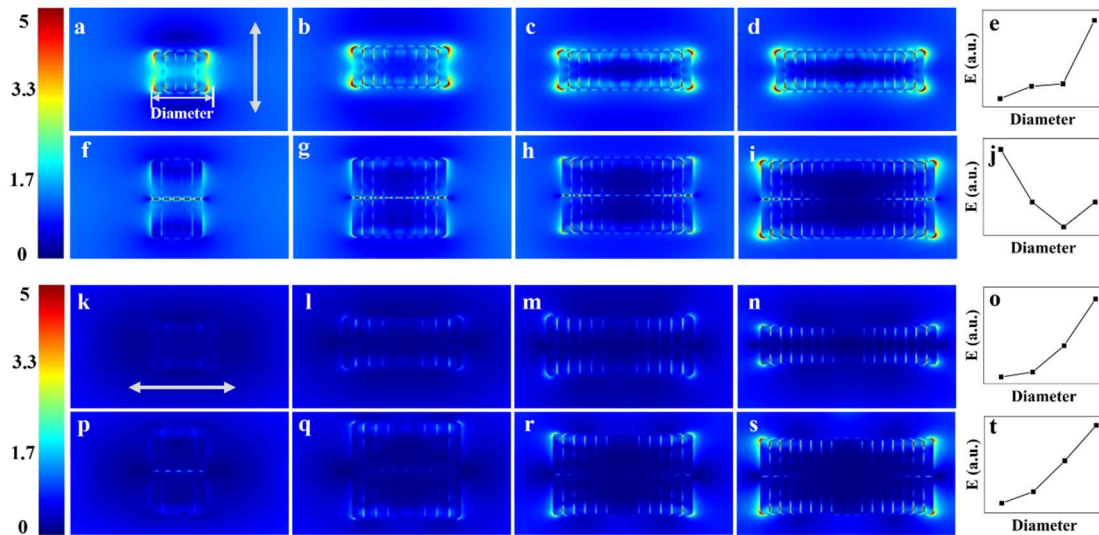


Figure S14 FDTD simulations of the electric field intensity in specific regions of superparticles. (a)-(d) Increasing number of GNRs in a single layer. (e) Graph of the relationship between diameter and electric field intensity. (f)-(i) Increasing number of GNRs in two layers. (j) Graph of the relationship between diameter and electric field intensity. (k)-(t) Same structures as (a)-(j) but with a different light polarization direction. In (a)-(j), the polarization direction of the light is parallel to the longitudinal axis of the gold nanorods, while in (k)-(t), the polarization direction is perpendicular to the longitudinal axis of the gold nanorods.

Table S1 Table of specific values for the size of superparticles assembled from lo-GNRs and the corresponding Raman signal intensity of Nile red.

Superpartical Diameter (μm)	Nile Red Raman signal strength
0.66	1090
0.87	3000
1.12	4300
1.32	7000
1.54	15000
2.7	22500
4.2	35000
4.76	75000
8	160000
9.35	200000

Table S2 Table of specific values for the size of superparticles assembled from hi-GNRs and the corresponding Raman signal intensity of Nile red.

Superpartical Diameter (μm)	Nile Red Raman signal strength
0.62	160
0.67	250
0.68	525
0.85	1400
1.24	4900
2.28	11000
2.57	12000
3.72	25000
6.1	30000
6.91	47250

Table S3 The highest electric field intensities simulated for each structure in Figure 5.

Number	Highest electric field strength	Number	Highest electric field strength
5a	10.1	5f	23.2
5b	10.2	5g	21.5
5c	9.1	5h	21.1
5d	10.7	5i	26.5

Number	Highest electric field strength	Number	Highest electric field strength
5k	2	5p	3.7
5l	2.3	5q	4.1
5m	4	5r	8.6
5n	7.2	5s	13.7

Table S4 The highest electric field intensities simulated for each structure in Figure S7.

Number	Highest electric field strength	Number	Highest electric field strength
S7a	6.8	S7f	14.1
S7b	8.01	S7g	12.2
S7c	8.26	S7h	11.3
S7d	14.5	S7i	12.2

Number	Highest electric field strength	Number	Highest electric field strength
S7k	1.96	S7p	2.4
S7l	2.29	S7q	4.07
S7m	4.06	S7r	8.55
S7n	7.19	S7s	13.7